

Article

# Three-Dimensional Mesoporous Ni-CeO<sub>2</sub> Catalyst for Dry Reforming of Methane

Huiyao Jin <sup>1</sup>, Yuanqiao Liu <sup>1</sup>, Lizhi Huang <sup>1</sup>, Yali Liu <sup>1</sup>, Sha Cui <sup>1</sup>, Hui Liu <sup>2</sup>, Jing Xu <sup>3,\*</sup> and Luhui Wang <sup>1,4,\*</sup> 

<sup>1</sup> Zhejiang Key Laboratory of Petrochemical Pollution Control, Zhejiang Ocean University, Zhoushan 316022, China; jinhuiyao@zjou.edu.cn (H.J.); liuyuanqiao@zjou.edu.cn (Y.L.); huanglizhi@zjou.edu.cn (L.H.); yaliliu@zjou.edu.cn (Y.L.); cuisha2019@zjou.edu.cn (S.C.)

<sup>2</sup> School of Food and Pharmaceutical, Zhejiang Ocean University, Zhoushan 316022, China; liuhui@zjou.edu.cn

<sup>3</sup> National Engineering Research Center for Marine Aquaculture, Zhejiang Ocean University, Zhoushan 316022, China

<sup>4</sup> National-Local Joint Engineering Laboratory of Harbor Oil and Gas Storage and Transportation Technology, Zhejiang Ocean University, Zhoushan 316022, China

\* Correspondence: jingxu@zjou.edu.cn (J.X.); wangluhui1008@zjou.edu.cn (L.W.)

**Abstract:** Using the colloidal solution combustion approach, a three-dimensional mesoporous 5%Ni-CeO<sub>2</sub>-M catalyst was developed, with Ni incorporated into the pores, and applied in the dry reforming of methane. Comprehensive characterization revealed that the 5%Ni-CeO<sub>2</sub>-M catalyst had a large specific surface area and a three-dimensional mesoporous structure. A rich Ni-CeO<sub>2</sub> interface was formed by closely spaced tiny CeO<sub>2</sub> and NiO nanoparticles within the spherical pore wall. With very little carbon deposition over a 100 h period at 700 °C, the catalyst showed excellent activity and stability. The tiny Ni nanoparticles, along with the substantial Ni-CeO<sub>2</sub> interfaces that make up this three-dimensional in-form mesoporous catalyst, are responsible for the outstanding effectiveness of this 5%Ni-CeO<sub>2</sub>-M catalyst.

**Keywords:** dry reforming of methane; Ni-CeO<sub>2</sub>; colloidal solution combustion; three-dimensional; mesoporous



**Citation:** Jin, H.; Liu, Y.; Huang, L.; Liu, Y.; Cui, S.; Liu, H.; Xu, J.; Wang, L. Three-Dimensional Mesoporous Ni-CeO<sub>2</sub> Catalyst for Dry Reforming of Methane. *Catalysts* **2024**, *14*, 291. <https://doi.org/10.3390/catal14050291>

Academic Editor: Inés Moreno García

Received: 31 March 2024

Revised: 17 April 2024

Accepted: 19 April 2024

Published: 26 April 2024



**Copyright:** © 2024 by the authors. Licensee MDPI, Basel, Switzerland. This article is an open access article distributed under the terms and conditions of the Creative Commons Attribution (CC BY) license (<https://creativecommons.org/licenses/by/4.0/>).

## 1. Introduction

The worldwide increase in the number of people and excessive energy consumption associated with our rapid societal progress have resulted in large-scale greenhouse gas emissions (CH<sub>4</sub> and CO<sub>2</sub>) that negatively impact the environment. Consequently, the issue of global warming caused by greenhouse gases has garnered attention worldwide. Therefore, a great deal of academics think that effective means of these two gases—ideally by turning them into useful products—is a crucial step toward mitigating the negative impacts of global warming [1]. Based on the aforementioned concepts, it can be concluded that the methane dry reforming reaction (DRM: CH<sub>4</sub> + CO<sub>2</sub> → CO + H<sub>2</sub>) is an extremely beneficial chemical reaction that can transform the two gases into a mixture of CO and H<sub>2</sub>, which is more suitable for industrial reactions [2,3]. Every nation in the world values this reaction much as it contributes significantly to the production and use of energy as well as the preservation of the environment [4–6].

Industrial catalysts should maintain high catalytic activity and a long service life throughout the production process, and at the same time, their cost must be considered. Therefore, the utilization of non-noble metal catalysts, which are low-cost, easily accessible, and exhibit excellent catalytic performance, has become the focal point of DRM research and development in recent years. Despite the extensive attention that Ni-based catalysts have received in DRM reactions due to their high catalytic activity [7–10], their inherent shortcomings cannot be overlooked. At high temperatures, Ni-based catalysts are susceptible to sintering, and carbon deposition forms on their surface. During this process, the

growth of carbon fibers destroys the pore structure of the catalyst, significantly reducing its reactivity and stability [11–14]. Simultaneously, in Ni-based catalysts, the interaction between Ni active components and the support, as well as the metal dispersion of Ni on the surface, are crucial factors determining the activity and stability of DRM. However, currently, most Ni-based catalysts employed for DRM are particle-supported, posing issues such as uneven distribution of Ni active components, low metal dispersion, a small specific surface area, and a limited number of exposed active sites, all of which hinder efficient DRM reactions. Furthermore, the weak interaction between Ni active sites and the support further diminishes metal dispersion and metal-support interaction, leading to carbon deposition and catalyst sintering in high-temperature DRM reactions. This ultimately deactivates the Ni-based catalyst, limiting its industrial application [15–18]. To address these challenges, it is often possible to modify the interface structure and performance of catalysts by introducing promoters or reducing the size of metal particles [19–21]. The catalytic performance is intimately linked to the size and dispersion of active metals. Smaller Ni particles not only possess a larger metal-support interface, which facilitates the dissociation of CO<sub>2</sub> into CO and adsorbed oxygen, but also promotes carbon oxidation [22,23]. Consequently, controlling the size of Ni particles to prevent carbon formation during high-temperature DRM reactions is crucial for enhancing catalyst activity and stability.

As is widely recognized, the strong contact that forms between the metal and oxide interface during catalyst preparation helps to both avert carbon deposition and augment the function of nickel-based catalysts in DRM operations [24,25]. Because of its exceptional oxygen storage and release capabilities, as well as its distinct redox properties, cerium dioxide has drawn the attention of several academics [26–28]. Oxygen vacancies can be produced in CeO<sub>2</sub> when Ce<sup>4+</sup> is converted to Ce<sup>3+</sup> [27]. As a result, the CO<sub>2</sub> in the reaction was adsorbed and dissociated more quickly [29]. Furthermore, a lot of studies employ the method of density functional theory (DFT) to compute and discover that in the presence of powerful metal-support interaction (SMSI) among Ni and CeO<sub>2</sub>, energy may be produced at a comparatively low temperature to facilitate the breaking of the C-H bonding [30,31]. The Ni-CeO<sub>2</sub> contact helps the DRM process by increasing the reaction rate and limiting carbon deposit production [28].

To enhance the performance of Ni-CeO<sub>2</sub> catalysts in DRM, researchers have utilized various preparation methods to produce Ni-CeO<sub>2</sub> catalysts with small Ni particles and rich Ni-CeO<sub>2</sub> interfaces. Ni particles were loaded onto CeO<sub>2</sub> nanosheets by Rood et al. [32], who found that these nanosheets could prevent active metals from aggregating, function well as catalysts, and resist sintering during DRM processes. Tang et al. [33] reported a Ni-CeO<sub>2</sub> catalyst with a core-shell structure demonstrated excellent catalyst activity and reliability in DRM processes. The CeO<sub>2</sub> shell prevents the accumulation and sintering of the Ni nanoparticles. After preparing Ni/CeO<sub>2</sub> catalysts using three techniques (sol-gel, self-combustion, and microemulsion) and applying them to DRM reactions, Yahi et al. [34] discovered that the self-combustion method had good activity, whereas the microemulsion method's catalyst did not exhibit activity as a catalyst in this catalytic test. Zhou et al. [35] successfully prepared a multi-layer Ni/CeO<sub>2</sub> catalyst using a simple and efficient one-pot hydrothermal synthesis method. This catalyst demonstrated a relatively stable coke formation rate along with excellent DRM reaction activity. These superior properties were primarily attributed to the strengthening of the metal-interface between the Ni phase and the CeO<sub>2</sub> phase, as well as the increase in weak alkaline sites on the catalyst surface. Kim et al. [36] employed two synthetic strategies and varying nickel loading to prepare a CeO<sub>2</sub> catalyst loaded with nickel nanoparticles (Ni-NP). Among these catalysts, the Ni-CeO<sub>2</sub>/7.5 catalyst, which was prepared using the one-pot method, exhibits excellent catalytic performance. The high activity and durability of this catalyst are attributed to the coke resistance of CeO<sub>2</sub>, its superior redox properties, the good dispersion of the active phase, and the strong interaction with the support.

Recently, there have been reports of a surface colloidal solution combustion method [37–39] for synthesizing three-dimensional mesoporous catalysts, which have large surface areas

and rich metal-support interfaces and can significantly enhance the catalytic performance. However, to the best of our knowledge, there have been no reports on the use of colloidal solution combustion to prepare three-dimensional mesoporous catalysts for methane dry-reforming reactions.

In this study, a three-dimensional mesoporous Ni-CeO<sub>2</sub>-M catalyst with excellent dispersibility was produced using a colloidal solution combustion approach. In the methane dry reforming reaction, this type of catalyst containing tiny Ni particles implanted in the pore walls demonstrated exceptional catalytic activity, serving as a model for further study.

## 2. Results and Discussion

### 2.1. Characterization of Catalysts

The XRD patterns of the freshly prepared and reduced samples are shown in Figure 1. The XRD spectra of the two catalysts and the, CeO<sub>2</sub>-M, prior to reduction are shown in Figure 1a. This image shows that both the new catalysts have distinctive CeO<sub>2</sub> diffraction peaks.

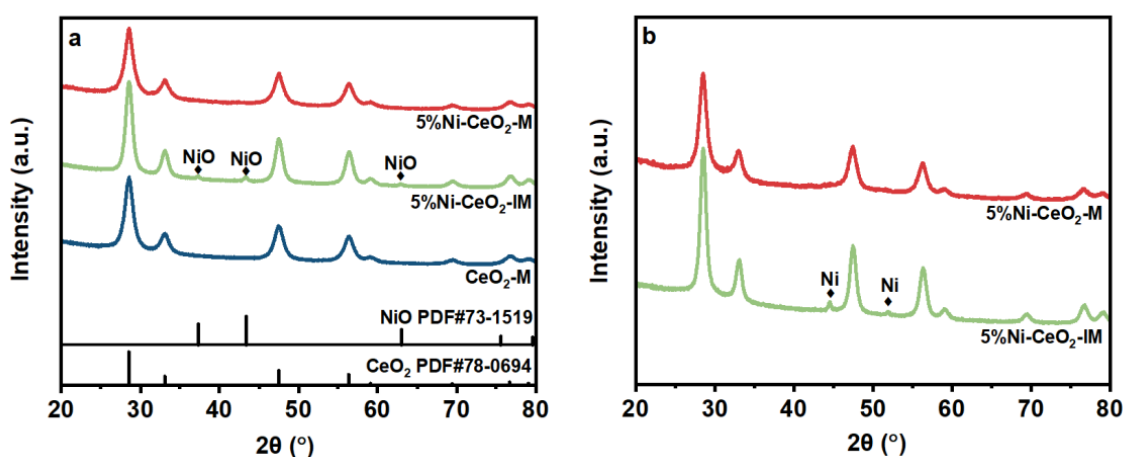


**Figure 1.** XRD patterns of the (a) calcined and (b) reduced CeO<sub>2</sub>-M, 5%Ni-CeO<sub>2</sub>-M, and 5%Ni-CeO<sub>2</sub>-IM catalysts.

The curve of the 5%Ni-CeO<sub>2</sub>-M catalyst in Figure 1a lacks any discernible diffraction peaks that can be definitively linked to NiO. This finding implies that there is no development of larger NiO particles in the microstructure of this catalyst. This behavior suggests that the Ni species are uniformly distributed throughout the catalyst matrix and form metal-oxide interfaces with CeO<sub>2</sub>. No distinctive NiO diffraction peaks were observed. These structural features significantly affect catalyst performance, particularly with regard to the surface reaction process and the movement of active species during catalytic reactions. NiO (NiO (111), (200), and (220) crystal layers) have three different distinctive peaks that are easily identifiable on the XRD curve of the 5%Ni-CeO<sub>2</sub>-IM catalyst [40]. This suggests that the scattered NiO particles on the CeO<sub>2</sub> surface formed NiO particles during calcinations. Given that larger particles might lower the specific surface area and catalytic activity of the catalyst, this aggregation event may have an impact on the catalyst's performance.

The lattice structure of the 5%Ni-CeO<sub>2</sub>-IM catalyst is shown in Figure 1b, where the metallic Ni diffraction peaks are clearly visible. This behavior may be explained by the fact that the larger NiO particles inside the catalyst transform into larger metallic Ni particles throughout the reduction process. Additional examination confirmed that the Ni-CeO<sub>2</sub>-M catalyst exhibited a greater dispersion of Ni than the other catalysts. The dispersion of Ni particles is one of the primary factors affecting the efficiency of the catalyst because a higher dispersion frequently translates into better catalytic activity and efficiency.

Figure 2 shows the N<sub>2</sub> adsorption/desorption isotherms and pore size distributions for CeO<sub>2</sub>-M, 5%Ni-CeO<sub>2</sub>-IM, and 5%Ni-CeO<sub>2</sub>-M. As shown in Figure 2a, all samples exhibited typical type-IV isotherms with hysteresis loops, indicating that these materials

had mesoporous structures. Figure 2b shows that the primary pore sizes of these catalysts were distributed between 20 and 22 nm, confirming the mesoporous structure formed by the etching of colloidal SiO<sub>2</sub> (approximately 22 nm) during catalyst preparation.

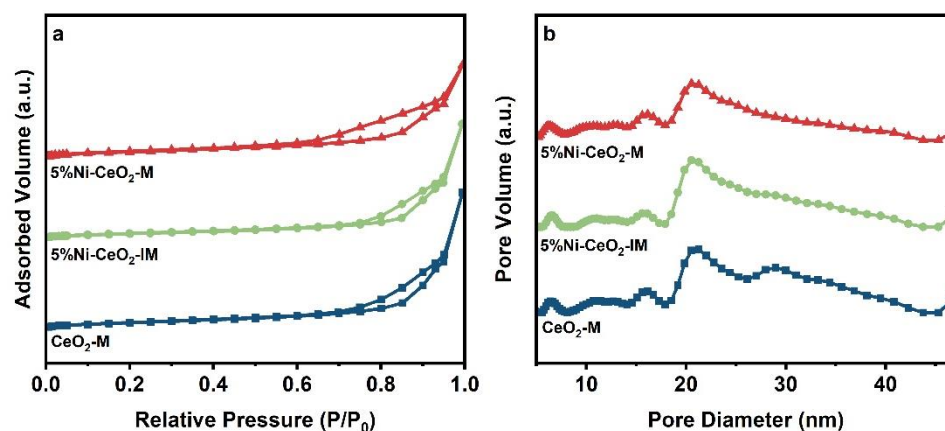


**Figure 2.** (a) N<sub>2</sub> adsorption–desorption isotherms and (b) pore size distributions of CeO<sub>2</sub>-M, 5%Ni-CeO<sub>2</sub>-IM, and 5%Ni-CeO<sub>2</sub>-M catalysts.

Table 1 highlights the physical and structural parameters of CeO<sub>2</sub>-M and the catalyst samples with 5%Ni-CeO<sub>2</sub>-M and 5%Ni-CeO<sub>2</sub>-IM. The solution made up of the cold combustion approach yielded specific surface areas of 105 m<sup>2</sup>/g for CeO<sub>2</sub>-M and 123 m<sup>2</sup>/g for 5%Ni-CeO<sub>2</sub>-M. The large specific surface areas of these two samples are outlined by the catalyst's mesopore structure and tiny particle size after SiO<sub>2</sub> etching. The high NiO particle size in the sample may have contributed to the significantly reduced specific surface area of the 5%Ni-CeO<sub>2</sub>-IM catalyst (80 m<sup>2</sup>/g).

**Table 1.** Physicochemical properties of CeO<sub>2</sub>-M, 5%Ni-CeO<sub>2</sub>-M, and 5%Ni-CeO<sub>2</sub>-IM.

Samples	S <sub>BET</sub> <sup>a</sup> (m <sup>2</sup> /g)	Pore Volume <sup>a</sup> (cm <sup>3</sup> /g)	CeO <sub>2</sub> Crystal Size <sup>b</sup> (nm)
CeO <sub>2</sub> -M	105	0.65	5.9
5%Ni-CeO <sub>2</sub> -M	123	0.46	5.8
5%Ni-CeO <sub>2</sub> -IM	80	0.55	6.4

<sup>a</sup> Measured using N<sub>2</sub> adsorption–desorption analysis. <sup>b</sup> XRD measurements calculated using Scherrer's formula.

TEM images of the 5%Ni-CeO<sub>2</sub>-M and 5%Ni-CeO<sub>2</sub>-IM catalysts are shown in Figure 3. Three-dimensional mesopores with diameters of approximately 20 nm were observed for the two catalysts (Figure 3a,c). Small NiO and CeO<sub>2</sub> grains were formed by the wall of the spherical pores that developed when SiO<sub>2</sub> was washed away with NaOH during the catalyst manufacturing procedure. In general, the mesopore diameter matches that of the colloidal SiO<sub>2</sub> component. As shown in Figure 3b, in the 5%Ni-CeO<sub>2</sub>-M catalyst, NiO particles of approximately 5 nm were confined to spherical pore walls by CeO<sub>2</sub>, and no noticeably large NiO particles were observed, suggesting that Ni species were highly distributed in the catalyst. This was consistent with the XRD results. As shown in Figure 3d, NiO particles of approximately 10 nm were deposited on the CeO<sub>2</sub> surface. These findings suggest that NiO in the 5%Ni-CeO<sub>2</sub>-M catalyst was embedded within the pore wall, and NiO and CeO<sub>2</sub> were highly dispersed in the pore wall. This creates an abundant Ni-CeO<sub>2</sub> interface, which is crucial for the DRM reaction.

H<sub>2</sub>-TPR was utilized in Figure 4 to illustrate the reducing behavior of the three samples. For the CeO<sub>2</sub>-M, two reduction peaks ( $\alpha$  and  $\theta$ ) were observed. The low-temperature reducing peak ( $\alpha$ ), which occurred between 300 and 650 °C, was attributed to the reduction in surface CeO<sub>2</sub> [41,42]. Conversely, the reduction in the bulk CeO<sub>2</sub> contributes to the appearance of the high-temperature reducing peak ( $\theta$ ), observed at approximately 780 °C [41,42].

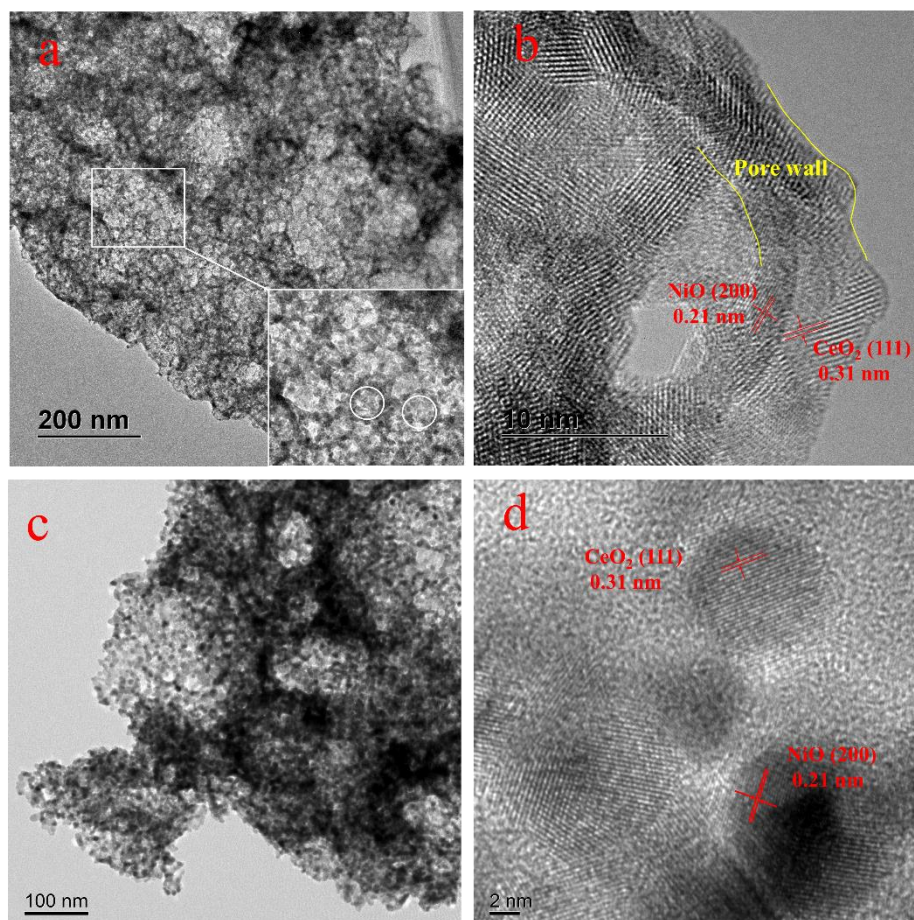


Figure 3. TEM images of fresh catalysts. (a,b) 5%Ni-CeO<sub>2</sub>-M and (c,d) 5%Ni-CeO<sub>2</sub>-IM.

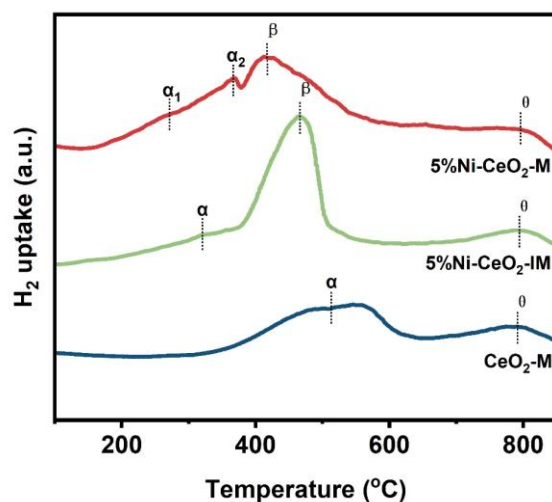


Figure 4. H<sub>2</sub>-TPR profiles of fresh CeO<sub>2</sub>, 5%Ni-CeO<sub>2</sub>-M, and 5%Ni-CeO<sub>2</sub>-IM catalysts.

We discovered that three different reduction peaks ( $\alpha$ ,  $\beta$ , and  $\theta$ ) were generated by both catalysts. The bulk phase reduction in CeO<sub>2</sub> was the cause of the reduced peak ( $\theta$ ) near 780 °C. The catalyst's surface CeO<sub>2</sub> and NiO particle reduction leads to the appearance of the  $\beta$  peak [43]. The dispersion of NiO on the CeO<sub>2</sub> surface is related to the location of the  $\beta$  peak. A larger degree of dispersion of NiO is indicated by a lower decrease in the temperature of the  $\beta$  peak [43]. The  $\beta$ -peak reduction temperatures of the two catalysts revealed that the reduction temperature of the 5%Ni-CeO<sub>2</sub>-M catalyst was lower than that

of the 5%Ni-CeO<sub>2</sub>-IM catalyst. This indicates that the Ni in the 5%Ni-CeO<sub>2</sub>-M catalyst was more dispersed.

For the 5%Ni-CeO<sub>2</sub>-M and 5%Ni-CeO<sub>2</sub>-IM catalysts, the  $\alpha$ ,  $\alpha_1$ , and  $\alpha_2$  peaks are assigned to the reduction peaks of oxygen adsorbed on the oxygen vacancies in CeO<sub>2</sub> [43–45]. The difference between the valence state of the metal and the ionic radius causes charge imbalance and distortion of the CeO<sub>2</sub> lattice, which leads to oxygen vacancies when Ni<sup>2+</sup> ions with smaller ions enter the lattice to replace Ce<sup>4+</sup> [44,45]. At low temperatures, H<sub>2</sub> may readily reduce the oxygen adsorbed on these vacancies. The  $\alpha$ -peak area of the 5%Ni-CeO<sub>2</sub>-M catalyst, including  $\alpha_1$  and  $\alpha_2$ , was considerably larger than that of the other catalysts, confirming that it had a greater number of oxygen vacancies. The DRM catalyst's strong activity and long-term stability are maintained by these plentiful oxygen vacancies that the catalyst creates, which are helpful for the reaction's activation and the removal of carbon species produced during the reaction [46]. According to the TPR result, the 5%Ni-CeO<sub>2</sub>-M catalyst showed highly dispersed NiO and more nickel ions entering the CeO<sub>2</sub> lattices, resulting in wealthier oxygen vacancies. Nonetheless, the NiO particles in the Ni-CeO<sub>2</sub>-IM catalyst were large, and very few oxygen vacancies formed there. This result is in agreement with the XRD results.

The surface structures of the two catalysts were further analyzed using XPS. As shown in Figure 5, the spectrum displays up to ten signal components resulting from various final electron configurations belonging to Ce 3d<sub>5/2</sub> and Ce 3d<sub>3/2</sub>. Among the ten peaks in the figure, six are attributed to Ce<sup>4+</sup> and four are attributed to Ce<sup>3+</sup> [47,48], indicating that both Ce<sup>3+</sup> and Ce<sup>4+</sup> exist in the catalysts simultaneously. Based on the findings of this investigation, when Ni is mixed with CeO<sub>2</sub>, an oxygen vacancy with a couple of electrons emerges to balance the charge mismatch between Ce<sup>4+</sup> and Ni<sup>2+</sup>, resulting in the buildup of Ce<sup>3+</sup>. One of the key elements influencing the DRM reaction's catalytic activity is Ce<sup>3+</sup> [4,48]. After calculating the peak areas of the two catalysts, we noticed that the proportional ratios of Ce<sup>3+</sup>/(Ce<sup>3+</sup> + Ce<sup>4+</sup>) from the 5%Ni-CeO<sub>2</sub>-M and 5%Ni-CeO<sub>2</sub>-IM catalysts were 21.93% and 18.30%, respectively. This indicates that the catalyst formed a greater number of oxygen vacancies because the 5%Ni-CeO<sub>2</sub>-M catalyst had a larger surface concentration of Ce<sup>3+</sup>.

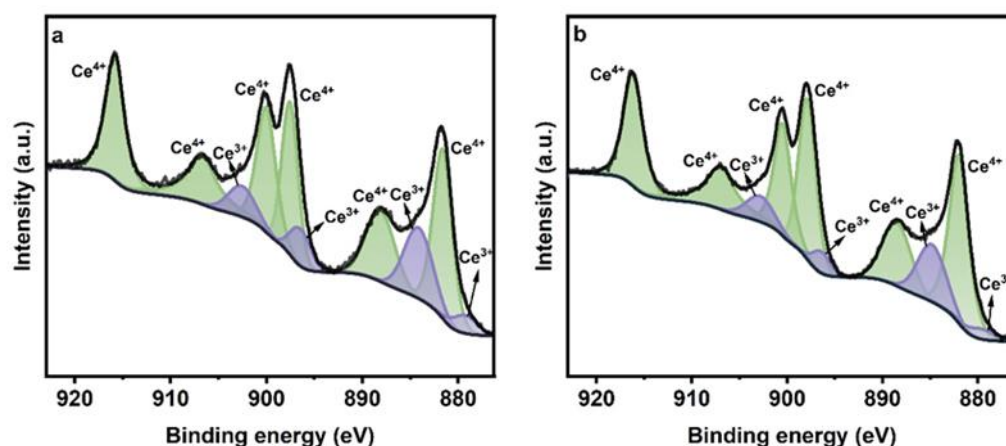
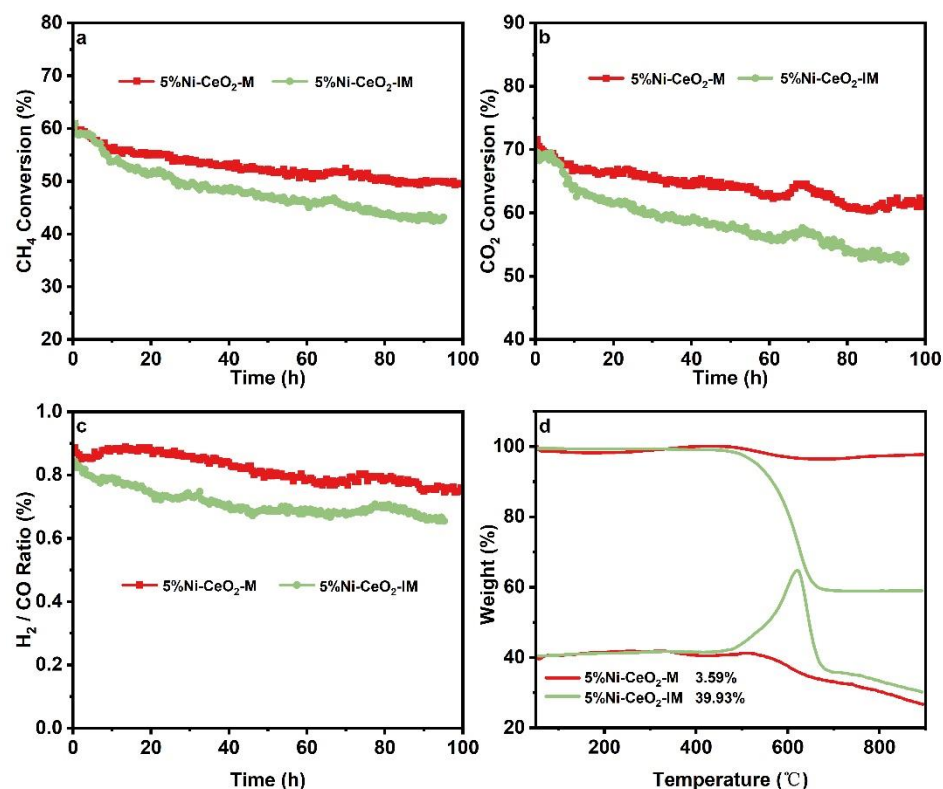


**Figure 5.** Ce 3d X-ray photoelectron spectroscopy (XPS) spectra of the catalysts: (a) 5%Ni-CeO<sub>2</sub>-M and (b) 5%Ni-CeO<sub>2</sub>-IM.

## 2.2. DRM Performances and Carbon Deposition over Catalysts

The efficiency of the catalytic process was evaluated at 700 °C and room temperature with a GHSV of 135 L/g<sub>cat</sub>/h. Figure 6a,b demonstrates that, in comparison with the other prepared catalysts, the 5%Ni-CeO<sub>2</sub>-M catalyst showed a higher rate of CH<sub>4</sub> and CO<sub>2</sub> transformation. The two catalysts initially exhibited similar CO<sub>2</sub> and methane conversion rates that gradually decreased as the reaction progressed. The 5%Ni-CeO<sub>2</sub>-M catalyst's CO<sub>2</sub> and CH<sub>4</sub> conversion decreased by only 10% after 100 h of reaction, whereas that of the

5%Ni-CeO<sub>2</sub>-IM catalyst decreased by 18% after 90 h. This highly dispersed Ni sintering and carbon deposition may be the reason for the gradual decline in the conversion rate.



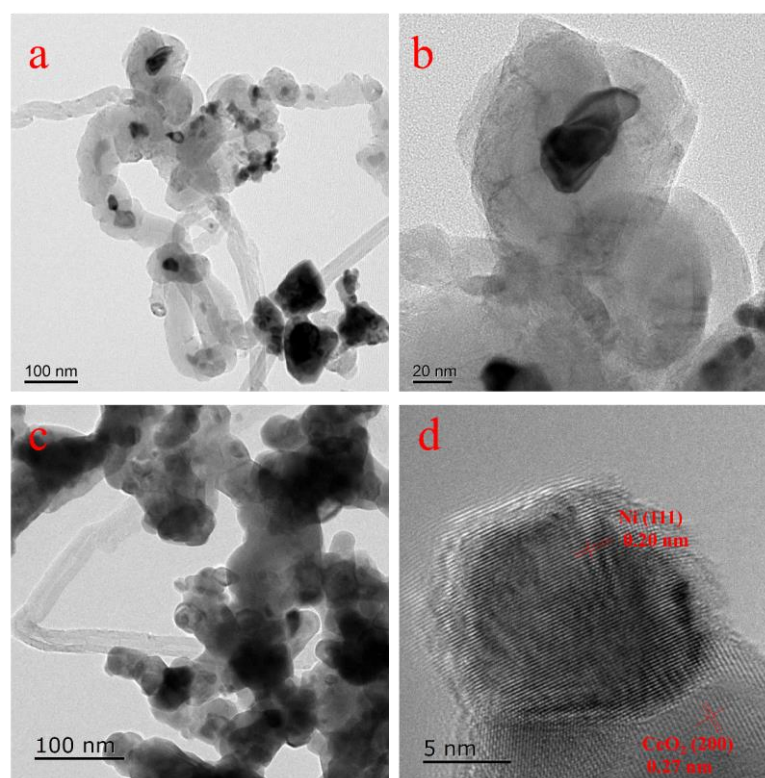
**Figure 6.** (a) CH<sub>4</sub> conversion, (b) CO<sub>2</sub> conversion, and (c) H<sub>2</sub>/CO ratio of 5%Ni-CeO<sub>2</sub>-M and 5%Ni-CeO<sub>2</sub>-IM catalysts during DRM. (d) TGA profiles of the spent catalysts.

Figure 6a,b demonstrate that the CO<sub>2</sub> conversions of both catalysts were higher than their CH<sub>4</sub> conversion rates, whereas Figure 6c indicates that the H<sub>2</sub>/CO ratios of both catalysts were less than 1. This indicates that the catalyst underwent a reverse water-gas shift process, consuming H<sub>2</sub> and CO<sub>2</sub> to generate CO and H<sub>2</sub>O [49].

The quantity of carbon deposited on the spent catalysts was quantified using TG, and the results are shown in Figure 6d. The oxidization of deposited carbon was the source of the notable weight loss (39.9%) of the 5%Ni-CeO<sub>2</sub>-IM catalyst between 500 and 700 °C. In contrast, after 100 h of performance testing, the 5%Ni-CeO<sub>2</sub>-M catalyst contributed only 3.6% of the weight decrease. This indicated that the 5%Ni-CeO<sub>2</sub>-M catalyst demonstrated strong resistance to carbon deposition.

The TEM images of the catalysts (5%Ni-CeO<sub>2</sub>-IM and 5%Ni-CeO<sub>2</sub>-M) following the reaction are depicted in Figure 7. We observed more carbon nanofibers and larger Ni particles on the spent 5%Ni-CeO<sub>2</sub>-IM catalyst (Figure 7a,b). A significant amount of nickel in this catalyst was sintered throughout the 100 h DRM process, as evidenced by the size range of 20–50 nm. The specific surface area of the catalyst was further decreased as a result of the severe sintering of the Ni particles, which lowered the activity of the catalyst and was detrimental to the long-term reaction study that will follow. Furthermore, we discovered that carbon nanofibers were produced in the catalyst following the reaction. The exposed metal surface area of the catalyst will not be affected by the creation of carbon nanofibers, but the catalyst's service life will be shortened, and the reactor will be blocked. In contrast, only a small amount of carbon nanofibers was observed on the spent 5%Ni-CeO<sub>2</sub>-M catalyst (Figure 7c). The Ni particles grew to a size of more than 10 nm following the reaction, as shown in Figure 7d; however, no carbon deposition was observed on the Ni nanoparticles in a close relationship with CeO<sub>2</sub>, highlighting the key role of the Ni-CeO<sub>2</sub> interface in preventing the accumulation of carbon on the catalyst. It is possible that the 5%Ni-CeO<sub>2</sub>-M

catalyst demonstrated better thermal stability because the Ni nanoparticles in it remained smaller after the reaction than those in the 5%Ni-CeO<sub>2</sub>-IM catalyst.



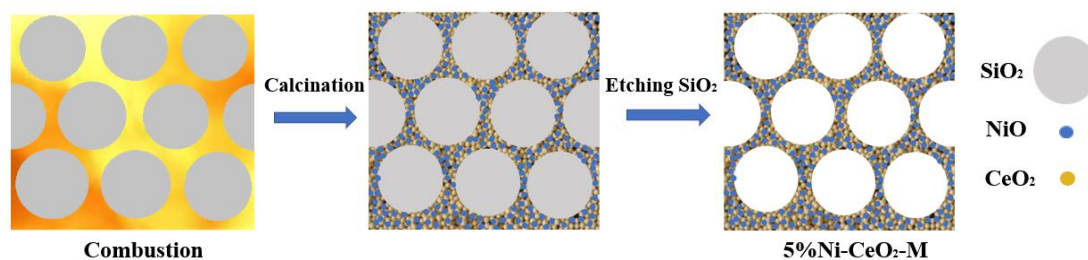
**Figure 7.** TEM images of spent catalysts. (a,b) 5%Ni-CeO<sub>2</sub>-IM and (c,d) 5%Ni-CeO<sub>2</sub> m.

After comparing the two catalysts, we discovered that the 5%Ni-CeO<sub>2</sub>-M catalyst exhibited superior thermal endurance and higher resistance to carbon deposition across the entire reaction period. This is because of the special pore-wall-confined catalyst structure, in which the catalyst pore walls form tiny, closely spaced particles of Ni and CeO<sub>2</sub>. One way that the smaller Ni particles help prevent the formation of carbon deposits throughout the reaction process. Concurrently, we discovered that an abundant Ni-CeO<sub>2</sub> interface formed in the 5%Ni-CeO<sub>2</sub>-M catalyst as a result of the tight contact between nickel and cerium dioxide. Because abundant surfaces efficiently hasten the carbon species' roasting during the reaction and lessen the amount of coke that is made [28]. Additionally, a three-dimensional pore-wall confined spatial structure can also alleviate the sintering of Ni particles and enhance their stability of Ni particles.

### 3. Materials and Methods

#### 3.1. Catalyst Preparation

A 5%Ni-CeO<sub>2</sub>-M catalyst was prepared using the colloidal solution combustion technique (Scheme 1). First, 0.722 g glycine, 2.523 g Ce(NO<sub>3</sub>)<sub>3</sub>·6H<sub>2</sub>O, and 0.261 g Ni(NO<sub>3</sub>)<sub>2</sub>·6H<sub>2</sub>O were uniformly dissolved. After that, 1.26 mL of silica sol (LUDO X TMA, 34 wt%, PH 4–7) was added for a 30 min ultrasonic treatment. The solution was heated to 180 °C on an electric heating plate. As heating progressed, the water in the solution gradually evaporated, and the remaining solids underwent combustion reactions to produce a yellowish-brown powder. The powder was then calcined for four hours at 700 °C in a muffle furnace. To obtain a 5%Ni-CeO<sub>2</sub>-M catalyst, the calcined powder was dissolved in a 2 mol/L NaOH solution, agitated in a water bath at 80 °C, and the water bath was stopped after 4 h. Using the same method, mesoporous CeO<sub>2</sub> was built and designated CeO<sub>2</sub>-M.



**Scheme 1.** Preparation of three-dimensional mesoporous 5%Ni-CeO<sub>2</sub>-M catalysts using colloidal solution combustion.

For comparison, we created a 5%Ni-CeO<sub>2</sub>-IM catalyst by impregnating previously synthesized CeO<sub>2</sub>-M with a nickel nitrate solution using the traditional impregnation technique. The catalysts with 5%Ni-CeO<sub>2</sub>-M and 5%Ni-CeO<sub>2</sub>-IM had nominal Ni concentrations of 5% by weight.

### 3.2. Catalyst Characterization

X-ray diffraction (XRD) was employed to identify the crystal phases of the catalyst samples. Measurements were conducted using a DX-2700BH diffractometer equipped with a Cu K $\alpha$  radiation source set at 30 kV and 40 mA. The diffraction patterns were collected over a 2 $\theta$  range of 20–80°.

Nitrogen adsorption–desorption isotherms were used to characterize the surface area and pore size distribution of the catalysts. Prior to analysis, samples underwent two preparatory steps: a vacuum treatment at 300 °C for 6 h to remove moisture and volatile contaminants. Measurements were performed at –196 °C using an Autosorb-iQ instrument (Quantachrome Instruments, Boynton Beach, FL, USA). The Brunauer-Emmett-Teller (BET) method was utilized to calculate the specific surface area of the catalyst. The non-local density functional theory (NLDFT) was employed to determine the pore size distribution and pore volume of the catalysts.

Hydrogen temperature-programmed reduction (H<sub>2</sub>-TPR) analysis was utilized to investigate the reduction properties of metal oxides within the catalyst. The analysis was performed using a TP-5080 instrument (Xianquan, Tianjin, China). A total of 50 mg of the catalyst was used for each test. Prior to the H<sub>2</sub>-TPR analysis, the catalyst was pretreated at 400 °C under a flow of argon gas at 20 mL/min for 15 min to remove any adsorbed impurities. The reduction tests were then conducted in a 5% H<sub>2</sub>/Ar mixture, maintaining a constant flow rate of 20 mL/min. The temperature ramp rate was set at 10 °C/min. A thermal conductivity detector (TCD) was employed to monitor the changes in gas composition, which indicates the reduction events in the catalyst.

X-ray photoelectron spectroscopy (XPS) was used to determine the elemental composition and stoichiometric ratios of the catalyst. Experiments were conducted on an EscaLab 250Xi instrument (Thermo Fisher Scientific, Waltham, MA, USA) using an Al K $\alpha$  radiation source, with binding energies calibrated against the C1s peak at 284.7 eV.

Transmission electron microscopy (TEM) provided high-resolution images of the catalyst structure. Samples were analyzed using a FEI TECNAI F30 microscope (FEI Company, Hillsboro, OR, USA).

Thermogravimetric analysis (TG) was conducted to assess the catalyst's thermal stability and decomposition behavior. The tests were carried out on an HCT-1 thermogravimetric analyzer (Henven Scientific Instrument, Beijing, China) with a temperature range of 20 to 900 °C, and the purge gas was air at a flow rate of 20 mL/min.

### 3.3. Catalytic Test

An 8 mm inner diameter fixed-bed quartz tube was used to evaluate the DRM efficiency of the catalyst. The catalyst (20 mg) was added to a reaction tube, and quartz wool was used to secure the two ends. A thermocouple of K variety was inserted into the catalyst

bed to assess the reaction temperature. The catalyst was reduced for 90 min at 700 °C in a mixture of 20% H<sub>2</sub> and N<sub>2</sub> before the reaction. 45 mL/min was the flow rate at which time the reaction gas (V(N<sub>2</sub>):V(CH<sub>4</sub>):V(CO<sub>2</sub>) = 1:1:1) had to go. There was a temperature of 700 °C at which the reaction occurred and a reaction time of 100 h. Throughout the reaction, the remaining gas was routed via a cold trap and fed into two GC-7900 gas chromatographs (Techcomp Scientific Instrument, Shanghai, China). These chromatographs were outfitted with a TCD and TDX-01 chromatography column, enabling a quantitative examination of the constructed catalyst.

#### 4. Conclusions

The colloidal solution combustion approach produced a 5%Ni-CeO<sub>2</sub>-M catalyst with an elevated surface space and a three-dimensional mesoporous structure. The Ni atoms in the hole walls of the Ni-CeO<sub>2</sub>-M catalyst were in close contact with CeO<sub>2</sub> and restricted by tiny CeO<sub>2</sub> particles. In contrast to the 5%Ni-CeO<sub>2</sub>-IM catalyst prepared using the traditional impregnation process, this led to higher stability and lower carbon deposition. The exceptional catalytic efficiency of the 5%Ni-CeO<sub>2</sub>-M catalyst was ascribed to its distinct mesoporous structure, in which tiny CeO<sub>2</sub> particles were in close proximity to the extensively scattered Ni particles. Small metals and CeO<sub>2</sub> nanoparticles make up the pore walls of three-dimensional mesoporous structures created by colloidal solution combustion, resulting in a multitude of metal-CeO<sub>2</sub> interactions that are critical to multiple processes.

**Author Contributions:** Conceptualization, L.W.; Funding acquisition, L.W.; Investigation, H.J., Y.L. (Yuanqiao Liu) and L.H.; Project administration, L.W.; Supervision, L.W.; Writing—original draft, H.J.; Writing—review and editing, Y.L. (Yali Liu), S.C., J.X., H.L. and L.W. All authors have read and agreed to the published version of the manuscript.

**Funding:** This work was supported by the Science and Technology Foundation of Zhoushan (2022C41002), Joint Funds of the Zhejiang Provincial Natural Science Foundation of China (LZY23B030-005), and Open Research Subject of the Zhejiang Key Laboratory of Petrochemical Environmental Pollution Control (2021Z01).

**Data Availability Statement:** The original contributions presented in the study are included in the article, further inquiries can be directed to the corresponding author.

**Conflicts of Interest:** The authors declare no conflicts of interest.

#### References

1. Alipour, Z.; Borugadda, V.B.; Wang, H.; Dalai, A.K. Syngas production through dry reforming: A review on catalysts and their materials, preparation methods and reactor type. *Chem. Eng. J.* **2023**, *452*, 139416. [[CrossRef](#)]
2. Shen, D.; Wang, J.; Bai, Y.; Lyu, S.; Zhang, Y.; Li, J.; Li, L.; Wang, G. Carbon-confined Ni based catalyst by auto-reduction for low-temperature dry reforming of methane. *Fuel* **2023**, *339*, 10. [[CrossRef](#)]
3. Zhou, D.; Huang, H.; Cai, W.; Liang, W.; Xia, H.; Dang, C. Immobilization of Ni on MOF-derived CeO<sub>2</sub> for promoting low-temperature dry reforming of methane. *Fuel* **2024**, *363*, 11. [[CrossRef](#)]
4. Jang, W.J.; Shim, J.O.; Kim, H.M.; Yoo, S.Y.; Roh, H.S. A review on dry reforming of methane in aspect of catalytic properties. *Catal. Today* **2019**, *324*, 15–26. [[CrossRef](#)]
5. Zhang, P.; Yang, X.J.; Hou, X.L.; Mi, J.L.; Yuan, Z.Z.; Huang, J.; Stampfl, C. Active sites and mechanism of the direct conversion of methane and carbon dioxide to acetic acid over the zinc-modified H-ZSM-5 zeolite. *Catal. Sci. Technol.* **2019**, *9*, 6297–6307. [[CrossRef](#)]
6. Ding, S.; Liu, Y.X. Adsorption of CO<sub>2</sub> from flue gas by novel seaweed-based KOH-activated porous biochars. *Fuel* **2020**, *260*, 10. [[CrossRef](#)]
7. Abdulrasheed, A.; Jalil, A.A.; Gambo, Y.; Ibrahim, M.; Hambali, H.U.; Hamill, M.Y.S. A review on catalyst development for dry reforming of methane to syngas: Recent advances. *Renew. Sust. Energ. Rev.* **2019**, *108*, 175–193. [[CrossRef](#)]
8. Li, S.Q.; Fu, Y.; Kong, W.B.; Pan, B.R.; Yuan, C.K.; Cai, F.F.; Zhu, H.; Zhang, J.; Sun, Y.H. Dually confined Ni nanoparticles by room-temperature degradation of AlN for dry reforming of methane. *Appl. Catal. B* **2020**, *277*, 10. [[CrossRef](#)]
9. Bai, Y.; Shen, D.; Yu, G.; Wang, J.; Lyu, S.; Zhang, Y.; Wang, G.; Li, J.; Li, L. Manufacture of highly loaded Ni catalysts by carbonization-oxidation-reduction for dry reforming of methane. *New J. Chem.* **2023**, *47*, 17186–17193. [[CrossRef](#)]
10. He, D.; Wu, S.; Cao, X.; Chen, D.; Zhang, L.; Zhang, Y.; Luo, Y. Dynamic trap of Ni at elevated temperature for yielding high-efficiency methane dry reforming catalyst. *Appl. Catal. B Environ. Energy* **2024**, *346*, 11. [[CrossRef](#)]

11. Song, Y.; Ozdemir, E.; Ramesh, S.; Adishev, A.; Subramanian, S.; Harale, A.; Albuali, M.; Fadhel, B.A.; Jamal, A.; Moon, D. Dry reforming of methane by stable Ni–Mo nanocatalysts on single-crystalline MgO. *Science* **2020**, *367*, 777–781. [[CrossRef](#)] [[PubMed](#)]
12. Shoji, S.; Peng, X.; Yamaguchi, A.; Watanabe, R.; Fukuhara, C.; Cho, Y.; Yamamoto, T.; Matsumura, S.; Yu, M.-W.; Ishii, S. Photocatalytic uphill conversion of natural gas beyond the limitation of thermal reaction systems. *Nat. Catal.* **2020**, *3*, 148–153. [[CrossRef](#)]
13. Zhu, Q.; Zhou, H.; Wang, L.; Wang, L.; Wang, C.; Wang, H.; Fang, W.; He, M.; Wu, Q.; Xiao, F.-S. Enhanced CO<sub>2</sub> utilization in dry reforming of methane achieved through nickel-mediated hydrogen spillover in zeolite crystals. *Nat. Catal.* **2022**, *5*, 1030–1037. [[CrossRef](#)]
14. Palmer, C.; Upham, D.C.; Smart, S.; Gordon, M.J.; Metiu, H.; McFarland, E.W. Dry reforming of methane catalysed by molten metal alloys. *Nat. Catal.* **2020**, *3*, 83–89. [[CrossRef](#)]
15. Niu, J.; Wang, Y.E.; Liland, S.K.; Regli, S.; Yang, J.; Rout, K.R.; Luo, J.; Rønning, M.; Ran, J.; Chen, D. Unraveling enhanced activity, selectivity, and coke resistance of Pt–Ni bimetallic clusters in dry reforming. *ACS Catal.* **2021**, *11*, 2398–2411. [[CrossRef](#)]
16. Haug, L.; Thurner, C.; Bekheet, M.F.; Bischoff, B.; Gurlo, A.; Kunz, M.; Sartory, B.; Penner, S.; Klötzer, B. Zirconium Carbide Mediates Coke-Resistant Methane Dry Reforming on Nickel-Zirconium Catalysts. *Angew. Chem. Int. Ed.* **2022**, *61*, 7. [[CrossRef](#)] [[PubMed](#)]
17. Ahn, S.; Littlewood, P.; Liu, Y.; Marks, T.J.; Stair, P.C. Stabilizing supported Ni catalysts for dry reforming of methane by combined La doping and Al overcoating using atomic layer deposition. *ACS Catal.* **2022**, *12*, 10522–10530. [[CrossRef](#)]
18. Guo, Z.; Chen, S.; Yang, B. Promoted coke resistance of Ni by surface carbon for the dry reforming of methane. *Isience* **2023**, *26*, 106237. [[CrossRef](#)] [[PubMed](#)]
19. Cao, A.N.T.; Nguyen, H.H.; Pham, T.-P.T.; Le Phuong, D.H.; Nguyen, N.A.; Vo, D.-V.N.; Pham, P.T. Insight into the role of material basicity in the coke formation and performance of Ni/Al<sub>2</sub>O<sub>3</sub> catalyst for the simulated-biogas dry reforming. *J. Energy Inst.* **2023**, *108*, 101252. [[CrossRef](#)]
20. Zhang, X.; Shen, Y.; Liu, Y.; Zheng, J.; Deng, J.; Yan, T.; Cheng, D.; Zhang, D. Unraveling the unique promotion effects of a triple interface in Ni catalysts for methane dry reforming. *Ind. Eng. Chem. Res.* **2023**, *62*, 4965–4975. [[CrossRef](#)]
21. Deng, J.; Bu, K.; Shen, Y.; Zhang, X.; Zhang, J.; Faungnawakij, K.; Zhang, D. Cooperatively enhanced coking resistance via boron nitride coating over Ni-based catalysts for dry reforming of methane. *Appl. Catal. B Environ.* **2022**, *302*, 10. [[CrossRef](#)]
22. Al-Fatesh, A.S.; Fakeeha, A.H.; Ibrahim, A.A.; Abasaed, A.E. Ni supported on La<sub>2</sub>O<sub>3</sub> + ZrO<sub>2</sub> for dry reforming of methane: The impact of surface adsorbed oxygen species. *Int. J. Hydrog. Energy* **2021**, *46*, 3780–3788. [[CrossRef](#)]
23. Zhang, M.; Zhang, J.; Zhou, Z.; Chen, S.; Zhang, T.; Song, F.; Zhang, Q.; Tsubaki, N.; Tan, Y.; Han, Y. Effects of the surface adsorbed oxygen species tuned by rare-earth metal doping on dry reforming of methane over Ni/ZrO<sub>2</sub> catalyst. *Appl. Catal. B Environ.* **2020**, *264*, 12. [[CrossRef](#)]
24. Suchorski, Y.; Kozlov, S.M.; Bepalov, I.; Datler, M.; Vogel, D.; Budinska, Z.; Neyman, K.M.; Rupprechter, G. The role of metal/oxide interfaces for long-range metal particle activation during CO oxidation. *Nat. Mater.* **2018**, *17*, 519–522. [[CrossRef](#)] [[PubMed](#)]
25. Gong, J.; Bao, X. Fundamental insights into interfacial catalysis. *Chem. Soc. Rev.* **2017**, *46*, 1770–1771. [[CrossRef](#)]
26. Lovell, E.C.; Großman, H.; Horlyck, J.; Scott, J.; Mädler, L.; Amal, R. Asymmetrical double flame spray pyrolysis-designed SiO<sub>2</sub>/Ce<sub>0.7</sub>Zr<sub>0.3</sub>O<sub>2</sub> for the dry reforming of methane. *ACS Appl. Mater. Interfaces* **2019**, *11*, 25766–25777. [[CrossRef](#)] [[PubMed](#)]
27. Teh, L.; Setiabudi, H.; Timmiati, S.; Aziz, M.; Anuar, N.; Ruslan, N. Recent progress in ceria-based catalysts for the dry reforming of methane: A review. *Chem. Eng. Sci.* **2021**, *242*, 116606. [[CrossRef](#)]
28. Yan, X.; Hu, T.; Liu, P.; Li, S.; Zhao, B.; Zhang, Q.; Jiao, W.; Chen, S.; Wang, P.; Lu, J. Highly efficient and stable Ni/CeO<sub>2</sub>-SiO<sub>2</sub> catalyst for dry reforming of methane: Effect of interfacial structure of Ni/CeO<sub>2</sub> on SiO<sub>2</sub>. *Appl. Catal. B* **2019**, *246*, 221–231. [[CrossRef](#)]
29. Omoregbe, O.; Danh, H.T.; Abidin, S.; Setiabudi, H.; Abdullah, B.; Vu, K.B.; Vo, D.-V.N. Influence of lanthanide promoters on Ni/SBA-15 catalysts for syngas production by methane dry reforming. *Procedia Eng.* **2016**, *148*, 1388–1395. [[CrossRef](#)]
30. Lustemberg, P.G.; Ramirez, P.J.; Liu, Z.; Gutierrez, R.A.; Grinter, D.G.; Carrasco, J.; Senanayake, S.D.; Rodriguez, J.A.; Ganduglia-Pirovano, M.V. Room-temperature activation of methane and dry re-forming with CO<sub>2</sub> on Ni-CeO<sub>2</sub>(111) surfaces: Effect of Ce<sup>3+</sup> sites and metal-support interactions on C-H bond cleavage. *ACS Catal.* **2016**, *6*, 8184–8191. [[CrossRef](#)]
31. Liu, Z.; Grinter, D.C.; Lustemberg, P.G.; Nguyen-Phan, T.D.; Zhou, Y.; Luo, S.; Waluyo, I.; Crumlin, E.J.; Stacchiola, D.J.; Zhou, J. Dry reforming of methane on a highly-active Ni-CeO<sub>2</sub> catalyst: Effects of metal-support interactions on C-H bond breaking. *Angew. Chem. Int. Ed.* **2016**, *55*, 7455–7459. [[CrossRef](#)] [[PubMed](#)]
32. Rood, S.C.; Ahmet, H.B.; Gomez-Ramon, A.; Torrente-Murciano, L.; Reina, T.R.; Eslava, S. Enhanced ceria nanoflakes using graphene oxide as a sacrificial template for CO oxidation and dry reforming of methane. *Appl. Catal. B Environ.* **2019**, *242*, 358–368. [[CrossRef](#)]
33. Tang, C.; Liping, L.; Zhang, L.; Tan, L.; Dong, L. High Carbon-Resistance Ni@ CeO<sub>2</sub> Core-Shell Catalysts for Dry Reforming of Methane. *Kinet. Catal.* **2017**, *58*, 800–808. [[CrossRef](#)]
34. Yahi, N.; Menad, S.; Rodríguez-Ramos, I. Dry reforming of methane over Ni/CeO<sub>2</sub> catalysts prepared by three different methods. *Green Process. Synth.* **2015**, *4*, 479–486. [[CrossRef](#)]
35. Zhou, R.F.; Mohamedali, M.; Ren, Y.X.; Lu, Q.Y.; Mahinpey, N. Facile synthesis of multi-layered nanostructured Ni/CeO<sub>2</sub> catalyst plus in-situ pre-treatment for efficient dry reforming of methane. *Appl. Catal. B Environ.* **2022**, *316*, 14. [[CrossRef](#)]

36. Kim, S.B.; Eissa, A.A.S.; Kim, M.J.; Goda, E.S.; Youn, J.R.; Lee, K. Sustainable Synthesis of a Highly Stable and Coke-Free Ni@CeO<sub>2</sub> Catalyst for the Efficient Carbon Dioxide Reforming of Methane. *Catalysts* **2022**, *12*, 22. [[CrossRef](#)]
37. Voskanyan, A.A.; Chan, K.-Y.; Li, C.-Y.V. Colloidal solution combustion synthesis: Toward mass production of a crystalline uniform mesoporous CeO<sub>2</sub> catalyst with tunable porosity. *Chem. Mater.* **2016**, *28*, 2768–2775. [[CrossRef](#)]
38. Voskanyan, A.A.; Ho, C.-K.; Chan, K.Y. 3D δ-MnO<sub>2</sub> nanostructure with ultralarge mesopores as high-performance lithium-ion battery anode fabricated via colloidal solution combustion synthesis. *J. Power Sources* **2019**, *421*, 162–168. [[CrossRef](#)]
39. Wang, L.; Liu, H. Mesoporous Co-CeO<sub>2</sub> catalyst prepared by colloidal solution combustion method for reverse water-gas shift reaction. *Catal Today* **2018**, *316*, 155–161. [[CrossRef](#)]
40. de la Cruz-Flores, V.G.; Martinez-Hernandez, A.; Gracia-Pinilla, M.A. Deactivation of Ni-SiO<sub>2</sub> catalysts that are synthesized via a modified direct synthesis method during the dry reforming of methane. *Appl. Catal. A* **2020**, *594*, 117455. [[CrossRef](#)]
41. Hong, W.; Zhang, L.; Miao, L.; Yuan, L.; Xue, B. Co/CeO<sub>2</sub> for ethanol steam reforming: Effect of ceria morphology. *J. Rare Earths* **2013**, *31*, 565–571.
42. Zhang, Y.; Wang, Z.; Zhou, J.; Cen, K. Ceria as a catalyst for hydrogen iodide decomposition in sulfur-iodine cycle for hydrogen production. *Int. J. Hydrog. Energy* **2009**, *34*, 1688–1695. [[CrossRef](#)]
43. Yisup, N.; Cao, Y.; Feng, W.-L.; Dai, W.-L.; Fan, K.-N. Catalytic oxidation of methane over novel Ce-Ni-O mixed oxide catalysts prepared by oxalate gel-coprecipitation. *Catal. Lett.* **2005**, *99*, 207–213. [[CrossRef](#)]
44. Shan, W.; Luo, M.; Ying, P.; Shen, W.; Li, C. Reduction property and catalytic activity of Ce<sub>1-x</sub>Ni<sub>x</sub>O<sub>2</sub> mixed oxide catalysts for CH<sub>4</sub> oxidation. *Appl. Catal. A* **2003**, *246*, 1–9. [[CrossRef](#)]
45. Shan, W.; Fleys, M.; Lapique, F.; Swierczynski, D.; Kiennemann, A.; Simon, Y.; Marquaire, P.-M. Syngas production from partial oxidation of methane over Ce<sub>1-x</sub>Ni<sub>x</sub>O<sub>2</sub> catalysts prepared by complexation-combustion method. *Appl. Catal. A Gen.* **2006**, *311*, 24–33. [[CrossRef](#)]
46. Wang, Y.; Zhang, R.; Yan, B. Ni/Ce<sub>0.9</sub>Eu<sub>0.1</sub>O<sub>1.95</sub> with enhanced coke resistance for dry reforming of methane. *J. Catal.* **2022**, *407*, 77–89. [[CrossRef](#)]
47. Kim, M.-J.; Youn, J.-R.; Kim, H.J.; Seo, M.W.; Lee, D.; Go, K.S.; Lee, K.B.; Jeon, S.G. Effect of surface properties controlled by Ce addition on CO<sub>2</sub> methanation over Ni/Ce/Al<sub>2</sub>O<sub>3</sub> catalyst. *Int. J. Hydrog. Energy* **2020**, *45*, 24595–24603. [[CrossRef](#)]
48. Jang, W.-J.; Kim, H.-M.; Shim, J.-O.; Yoo, S.-Y.; Jeon, K.-W.; Na, H.-S.; Lee, Y.-L.; Jeong, D.-W.; Bae, J.W.; Nah, I.W. Key properties of Ni-MgO-CeO<sub>2</sub>, Ni-MgO-ZrO<sub>2</sub>, and Ni-MgO-Ce(1-x)Zr(x)O<sub>2</sub> catalysts for the reforming of methane with carbon dioxide. *Green Chem.* **2018**, *20*, 1621–1633. [[CrossRef](#)]
49. Das, S.; Ashok, J.; Bian, Z.; Dewangan, N.; Wai, M.; Du, Y.; Borgna, A.; Hidajat, K.; Kawi, S. Silica-Ceria sandwiched Ni core-shell catalyst for low temperature dry reforming of biogas: Coke resistance and mechanistic insights. *Appl. Catal. B* **2018**, *230*, 220–236. [[CrossRef](#)]

**Disclaimer/Publisher’s Note:** The statements, opinions and data contained in all publications are solely those of the individual author(s) and contributor(s) and not of MDPI and/or the editor(s). MDPI and/or the editor(s) disclaim responsibility for any injury to people or property resulting from any ideas, methods, instructions or products referred to in the content.